Title: Macaque Brainnetome Atlas with Fine-grained Parcellations and Reliable Connections

Authors: Yuheng Lu[1,2†], Yue Cui[1,3†], Long Cao[4†], Luqi Cheng[1,10,12], Changshuo Wang[1,3,11], Youtong Liu[1,2], Baogui Zhang[1,3,5], Haiyan Wang[1], Kaixin Li[1,9], Liang Ma[1,2], Weiyang Shi[1,2], Wen Li[1,3], Zhenwei Dong[1,2], Yawei Ma[1,3,11], Zongchang Du[1,2], Hui Xiong[1], Na Luo[1], Yanyan Liu[1], Xiaoxiao Hou[1], Xinyi Liu[1,2], Hongji Sun[1], Jiaojian Wang[8], George Paxinos[7], Zhengyi Yang[1*], Lingzhong Fan[1,2,5*], Tianzi Jiang[1,2,5,12*]

Affiliations:

[1] Brainnetome Center, Institute of Automation, Chinese Academy of Sciences, Beijing 100190, China.

[2] School of Artificial Intelligence, University of Chinese Academy of Sciences, Beijing 100049, China.

[3] University of Chinese Academy of Sciences, Beijing 100049, China.

[4] Key Laboratory for NeuroInformation of the Ministry of Education, School of Life Science and Technology, University of Electronic Science and Technology of China, Chengdu 610054, China

[5] CAS Center for Excellence in Brain Science and Intelligence Technology, Institute of Automation, Chinese Academy of Sciences, Beijing 100190, China.

[6] State Key Laboratory of Brain and Cognitive Sciences, Beijing MRI Center for Brain Research, Institute of Biophysics, Chinese Academy of Sciences, Beijing 100190, China

[7] Neuroscience Research Australia and The University of New South Wales, Sydney, NSW 2031, Australia

[8] State Key Laboratory of Primate Biomedical Research, Institute of Primate Translational Medicine, Kunming University of Science and Technology, Kunming 650500, China

[9] School of Mechanical and Power Engineering, Harbin University of Science and Technology, Harbin 150080, China

[10] School of Life and Environmental Sciences, Guilin University of Electronic Technology, Guilin 541004, China

[11] Sino-Danish College, University of Chinese Academy of Science, Beijing 100049, China.

[12] Research Center for Augmented Intelligence, Zhejiang Lab, Hangzhou 311100, China

Corresponding Authors:

*Professor Tianzi Jiang, Brainnetome Center, Institute of Automation, Chinese Academy of Sciences, Beijing 100190, China. (Email: jiangtz@nlpr.ia.ac.cn)

*Professor Lingzhong Fan, Brainnetome Center, Institute of Automation, Chinese Academy of Sciences, Beijing 100190, China. (Email: lingzhong.fan@nlpr.ia.ac.cn)

*Associate Professor Zhengyi Yang, Brainnetome Center, Institute of Automation, Chinese Academy of Sciences, Beijing 100190, China. (Email: zhengyi.yang@nlpr.ia.ac.cn)

[†] The authors contribute equally

Authors Contributions

T.J. proposed the concept and designed the protocol. Y.L., Y.C., L.C., performed experiments and analyzed data. H.S., Y.L., H.X., and X.L. prepared the ex vivo samples, and B.Z. performed the MRI scanning. C.W and Z.Y. developed the website. G.P., L.F., and Y.L. contributed to the nomenclature. T.J., L.F., and Z.Y. led the project and supervised the experiments. All authors contributed to the writing of the manuscript.

Abstract

The rhesus macaque (*Macaca mulatta*) is a crucial experimental animal that shares many genetic, brain organizational, and behavioral characteristics with humans. A macaque brain atlas that identifies anatomically and functionally distinct regions is fundamental to biomedical and evolutionary research. However, even though connectivity information is vital for understanding brain functions, a connectivity-based whole-brain atlas of the macaque has not previously been made. In this study, we created a new whole-brain map, the Macaque Brainnetome Atlas, based on the anatomical connectivity profile provided by high-resolution angular and spatial diffusion MRI data. The new atlas consists of 248 cortical and 56 subcortical regions as well as their structural

and resting-state functional connections. We systematically evaluated the parcellations and connections using multi-site and multi-modal datasets to ensure reproducibility and reliability. The resulting resource, which is downloadable from http://atlas.brainnetome.org, includes (1) the thoroughly delineated Macaque Brainnetome Atlas (MacBNA), (2) the multi-modal connections, (3) the largest postmortem high resolution macaque dMRI dataset, and (4) ex vivo MRI, block-face, and Nissl-stained images obtained from a different macaque. We provide an exemplar use of the resource with a joint multi-modal and multi-scale utilization of MRI and Nissl data with our atlas as a reference system. The goals of the resource are not only to provide a backbone of the mesoscopic connectivity and a multi-omics (such as transcriptomes and proteomes) atlas but also to facilitate translational medicine, cross-species comparisons, and computational modelling, enriching the collaborative resource platform of nonhuman primate data.

Keywords: *Macaca mulatta, brain atlas, connectivity-based parcellation, diffusion MRI, resting functional connectivity, cytoarchitecture*

Abbreviation

IPL	*inferior parietal lobe*
IPS	*intraparietal sulcus*
IPLgr	*inferior parietal lobule, gyral rostral part*
IPLgri	*inferior parietal lobule, gyral rostrointermediate part*
IPLgci	*inferior parietal lobule, gyral caudointermediate part*
IPLgc	*inferior parietal lobule, gyral caudal part*
PM	*premotor cortex*
PMrd	*premotor cortex, rostrodorsal part*
PMcd	*premotor cortex, caudodorsal part*
PMi	*premotor cortex, intermediate part*
PMcv	*premotor cortex, caudoventral part*
PMrv	*premotor cortex, rostroventral part*
PMmr	*premotor cortex, rostromedial part*
PMcm	*premotor cortex, caudomedial part*
STG	*superior temporal gyrus*
CG	*cingulate cortex*

CGdc	*cingulate cortex, dorsocaudal part*
M1	*primary motor cortex*
OrG	*orbital gyrus*
FP	*frontal pole*
FPv	*frontal pole, ventral part*
FPd	*frontal pole, dorsal part*
6DC	*area 6 of cortex, dorsocaudal part*
6DR	*area 6 of cortex, dorsorostral part*
6M	*area 6 of cortex, medial*
6VC	*area 6 of cortex, ventrocaudal part*
6VR	*area 6 of cortex, ventrorostral part*

Introduction

Rhesus macaques have been widely employed to explore the mechanisms of human cognitive functions and to model human brain disorders due to their high similarity in genetics, physiology, and brain structure[1,2]. International brain projects[3–5] utilize non-human primate research as a core factor for elucidating the neural basis of cognition and for promoting translational medicine. A brain atlas that delineates the heterogeneous spatial organizations of the brain can provide a link that can be used to translate findings from non-human primates to humans. It can characterize distinct regional profiles, including connectivity, architecture, and topography[6,7], and is fundamental to understanding the function, development, and evolution of the brain[8]. The profiles of different brain regions measured by MRI, tracers, and histology uncover the diverse neurobiological properties across several levels, leading to a unifying map at multiple scales and a comprehensive validation of brain parcellations[9–11]. However, it is still challenging to delineate the macaque brain at multiple levels given its complicated organization.

Macaque brain cartography has as long a history as that of humans[12], and some researchers created macaque brain atlases in past decades[13–16]. Previous cyto-, myelo-, and chemoarchitectonic delineations of the macaque brain were primarily developed using neuroanatomical methodologies, and the boundaries of the brain structures were determined by microstructural anatomical features[14–19]. Unlike traditional histological methods, animal MRI allows for the intact measurement of the brain. Connectivity-based parcellations have emerged to segregate

the brain into distinct regions using diffusion and functional MRI[20,21]. Since anatomical connections are predictors of functional activations from the primary somatosensory[22,23] to the high-order association cortices[24], identifying the functional diversity of brain regions has been constrained by the unavailability of anatomical connections[25]. Anatomical connectivity-based techniques capture global properties by estimating the physical connections between regions, allowing for a more effective characterization of both the areal- and network-level organizations[7]. Accumulating evidence suggests that integrating anatomical connectivity with multi-modal information such as cytoarchitecture and tracers may be vital for elucidating the specialization of brain regions at multiple levels and scales[10,11,26]. To the best of our knowledge, a macaque whole-brain atlas based on anatomical connectivity has, until now, been unavailable.

Comprehensive atlases have successfully delineated brain regions based on anatomical connectivity profiles in other primates, specifically humans and marmosets[27,28]. In rhesus macaques, previous studies using anatomical connectivity to define functional borders mainly focused on particular regions, including the prefrontal cortex[29], inferior parietal lobule[30], and accumbens[31] nucleus and other areas[32,33]. Before the current study, an entire brain atlas of macaques based on anatomical connectivity had not yet been achieved. As a result of the limited scan tolerance of macaques in vivo, we collected high quality postmortem diffusion MRI (dMRI) data to provide a high spatial and angular resolution, something that would not have been possible in an in vivo study. The greater amount of time available in the postmortem study allows for a more precise characterization of connectivity profiles between regions[34,35], which benefits connectivity-based parcellations. The relationship between connection-based and cytoarchitecture-based parcellations has rarely been explored although some studies have implied that they converge in some brain regions[9,29,36]. MRI and Nissl-stained sections of a single monkey utilized in this study could not only help to validate the connectivity-based parcellation at a cellular level but could also provide microscopic properties such as cytoarchitecture and the glial framework[37].

In the current study, we present a fine-grained anatomical connectivity-based brain atlas of macaques, the Macaque Brainnetome Atlas (MacBNA), using high spatial and angular resolution dMRI images of 8 postmortem monkeys acquired with an ultra-high field 9.4T MRI scanner. We replicated the Macaque Brainnetome Atlas parcellation using an independent open public ex vivo macaque brain dataset. The anatomical connections from the postmortem dMRI data were validated by comparisons with invasive tracer data, the gold standard for connections. We also present a set of Nissl-stained sections from another monkey

brain to validate the MacBNA with a cytoarchitectonic analysis and to reconstruct the fiber orientation in white matter areas at a meso-scale level using the glia framework. We will release the resource, including the MacBNA and the corresponding multi-modal connectomes, the postmortem monkey dMRI data, the block-face images, and the histological sections, for open access.

Results

Diffusion MRI data with high angular and spatial resolution from eight ex vivo monkeys (Brainnetome-8) were collected to construct the Macaque Brainnetome Atlas. The whole brain was first delineated into 29 initial seed units and then each one was parcellated into multiple subdivisions based on its connectivity with the optimal cluster number determined by three cluster indices (Figs. 1 A-F). The whole brain of the macaque was finally divided into 248 cortical and 56 subcortical subregions with each hemisphere having an equal number of regions (Figs. 2A, B). The detailed parcellation of each seed region can be found in the Supplemental Results, and the nomenclature of the macaque atlas is in the Supplemental Nomenclature. An openly available ex vivo dataset, Oxford-I, was used to validate the parcellation scheme (Fig. 4A). The observed consistency using Cramér's V coefficient for the whole brain was 0.84 for the left hemisphere and 0.80 for the right (Fig. 4B). More than half the 29 initial regions had a consistency coefficient greater than 0.8 for both hemispheres.

The Nissl-stained sections of another ex vivo monkey was acquired following the protocol in Fig. 1G and were used to extract the cytoarchitecture of the regions in the MacBNA and to estimate the fiber orientation under a glial framework[37]. The cyto-boundary was then delineated based on the density profile obtained from the cytoarchitecture to validate the parcellations of our atlas at a microstructure level. The glial framework permitted orientation fitting and tractography at a mesoscopic resolution (44 microns in this study) and allowed for the reconstruction of tiny fiber structures, such as U-fibers, which could provide validation for traditional MRI techniques.

An Exemplar Region Analysis

Taking the premotor cortex (PM) as a representative instance, we identified seven subregions, the PMrd, PMcd, PMi, PMcv, PMrv, PMrm, and PMcm, according to the peak positions of their clustering indices (Fig. S2A)

(Fig. 3A, left panel), resulting in two more subdivisions than Paxinos et al.'s atlas (Fig. 3A, middle panel), which was defined based on cytoarchitecture. A pairwise Dice coefficient between each pair of areas was calculated to represent the extent of overlap and to quantify the similarity between the two different parcellations (Fig. S2A). On one hand, the PMrd, PMcv, and PMrv had high respective overlaps with the 6DR, 6VC, and 6VR areas of Paxinos et al.'s atlas in that their Dices exceeded 0.65, showing their correspondence with each other. On the other hand, the other two premotor regions of Paxinos et al.'s atlas, 6M and 6DC, were each segregated into two separate subregions in the MacBNA, i.e., 6M was subdivided into PMrm and PMcm and 6DC into PMcd and PMi. The structural connectivities of the PMcd and PMi (Fig. 3A, right panel) show the differences in their connection patterns with the whole brain. Specifically, the PMcd showed stronger connections with the medial cortex and posterior intraparietal regions and the PMi had stronger connections with the ventral premotor and sensorimotor areas. In addition, a seed correlation analysis of the PMcd and PMi using resting-state fMRI data revealed the divergence in functional connectivity between those two regions (Fig. S2B).

A gradient analysis using a diffusion embedding algorithm[38] based on the structural and functional connectivity of this premotor region shows that the first gradients of the two modalities had a high correlation coefficient ($r = 0.98$, $P < .001$, Figs. 3B, C). For the second and the third gradients, the correlations decreased to $r = 0.689$ ($P < .001$) and $r = 0.205$ ($P < .001$), respectively (Figs. S2C, D). A 2D visualization of the gradients using t-SNE[39] for each subregion presented a clear clustering pattern for both the structural and functional modalities, implying the reasonableness of our parcellations from the viewpoint of gradients.

To explore the cytoarchitectonic variations between those two regions, we collected Nissl-stained sections from a postmortem monkey (ID: R04) and mapped the MacBNA parcellation to the corresponding Nissl slice space (Fig. 3D) with the black boundary delineating the subregions of MacBNA in the left hemisphere and the orange and white dots marking the respective locations of the PMi and PMcd. The density profiles of those two regions (marked as box A in Figs. 3D, F) along the pial and white surfaces was extracted to obtain the boundary based on cytoarchitecture. A sliding window procedure was used to calculate the distance between the neighboring blocks (see Methods for details). The distance function of the profile positions located the maximal point as a peak with the block size set at 20. The block size was set from 11 to 24 to ensure that the maxima were robust and independent of this parameter (Fig. S3A). A Hotelling's T^2 test was used to confirm the

significance of the peak ($P < .05$), and the two neighboring sections underwent the same procedure to ensure that the peak location was stable and not a false positive due to artifacts and outliers (Figs. S3B, C). The cyto-boundary based on the profile density analysis (position 81, red line in Fig. 3E left panel) was close to the boundary determined by the connectivity (purple line). Fig. 3E (middle panel) shows the mean density profiles of PMcd and PMi from the pial to the gray/white surface. A permutation test (5000 samples) was utilized to test the significance of the difference in density profiles between the two subregions ($t = 17.4$, $P < .001$, Fig. 3E). A detailed laminar structure of a column of each subregion (Fig. 3E right panel) shows that column A, which was selected from the PMi (as marked with arrows in Fig. 3D), had a denser layer III while column B, which was selected from the PMcd, had larger pyramidal cells in layer III. The different aspects of the cytoarchitectonic analysis collectively explained our connectivity-based parcellation at a biological level.

The glial framework allows for an estimation of the orientation of the fibers in the white matter at a high spatial resolution (44 microns in our study) and could be used for tracking tiny tracts like U-fibers that might not be reconstructed directly via MRI due to the partial volume effect. Fig. 3F shows the principal orientation organization that was encoded by the RGB color of the stained section using the glial framework, which delineated the anatomical structures of major tracts such as the corpus callosum (CC) along the left-right axis and the external capsule (EC) along the inferior-superior axis (Fig. 3F). A qualitive comparison of the fitting orientation between the DTI and glial framework revealed their consistency in some major tracts (Fig. S7). A tiny tract was reconstructed directly via the glial framework that connected the neighboring gyral regions when seeded from the area below the sulci (marked in box B in Fig. 3F). Constructing the glial framework takes advantage of the high resolution of the Nissl sections and may be useful as a complement to dMRI.

Structural and Resting Functional Connectome

Our atlas of the macaque was mapped onto CIVM volume space and NMT volume space before separately constructing the structural connectome (Fig. 4C) for the two ex vivo datasets and the in vivo dataset. All the edges were kept without any threshold for the purpose of the subsequent analysis and online sharing (Fig. S10-S12). The cross-validation of our connectomes (Fig. 4C) showed a high correlation of $r = 0.98, 0.94, 0.95$ for each pair, demonstrating the high reproducibility for both the ex vivo and in vivo subjects. The correlation

coefficient between the two ex vivo datasets was larger than the one between the ex vivo and the in vivo, indicating greater consistency in the subjects under the same condition.

After using a custom fMRI preprocess pipeline that was adapted from a previous study[19], resting fMRI images from an in vivo cohort of 20 subjects were utilized to construct the resting functional connectome (Fig. S13-S15). In addition, we conducted a conventional seed-based correlation analysis (P = .01, FDR corrected) on the posterior cingulate cortex region (CGdc) of our atlas, to locate the most correlated region. The map (Fig. S16) includes the posterior cingulate, medial parietal cortex (PMC), dorsolateral prefrontal cortex (dlPFC), medial prefrontal cortex (mPFC), and temporal parietooccipital associated area (TPO), which together are similar to the default mode network found in previous studies[38,40,41].

Correspondence with Connectomes Constructed using Tracer Data

To reveal the level of agreement of the structural connectome with those derived from tracer data, an approximate comparison was made based on the mapped tracer connection from a published tracer study that had 29 injection sites[35,42]. Figs. 5A and 5B respectively show the tracer connections of areas 10 and 46v where two of the 29 injection sites were located. The 29 injection sites were mapped to our atlas since the original targets were identified in Markov et al.'s atlas[42], which has 91 areas. The Pearson coefficients of correlation were 0.71 and 0.42 between the mapped tracer connections and the dMRI-based connections of the FPv and FPd, respectively (Figs. 5A, B). As expected, the comparison introduced some false positive connections because of different boundaries between the two atlases. The connectional discrepancy between FPv and FPd captured by dMRI indicated that FPd had more connections with the dorsal frontal cortex and parietal cortex, whereas FPv had more connections with the temporal cortex and orbital frontal cortex, findings which are consistent with tracer data (Fig. 5C). The connection matrix of the 20 selected regions indicates that the dMRI and tracer data had similar patterns, as indicated by a moderate Pearson's correlation coefficient of $r = 0.63$, $P < 10^{-6}$.

Discussion

The Macaque Brainnetome Atlas is an accurately and effectively delineated whole-brain atlas of macaques based on which various profiles of brain regions were characterized at different levels using multi-modal and multi-scale data integrated into a unifying map[10,43–45]. The MacBNA consists of 248 cortical and 56 subcortical subregions identified by anatomical connectivity obtained from acquired high angular and spatial resolution dMRI data from an extensive ex vivo cohort of 8 macaques. The independent validation with open-access dMRI and tracer data of macaques revealed the reproducibility and validity of our parcellations and their connections. The regional boundaries based on the connectivity were found to be consistent with the cytoarchitectonic boundaries, which were drawn using the Nissl-stained histological images. The new atlas, multi-modal connectomes, and the acquired dMRI and Nissl data will be released as a resource to provide new opportunities for linking multi-modal data such as MRI, tracers and histological images at micro-, meso-, and macroscopic scales[46] with MacBNA as a reference system and to promote progress in translational medicine, cross-species comparative investigations, and computational models.

Macaque Brainnetome Atlas: Parcellation and Connection

Anatomical connectivity based on dMRI allows for a fast, efficient, and biologically meaningful construction of a 3D brain atlas with the tissue intact. Compared with 2D cytoarchitectonic parcellations based on labor-extensive stained sections, it avoids 3D reconstructions obtained by aligning 2D slices that need extensive registration and many computations. Anatomical connectivity is able to delineate a similar parcellation to that of traditional histological architecture although the techniques and methodologies differ from each other. Some studies found that the boundaries identified by the anatomical connections between brain areas conform to some degree to the histological subdivisions of the cortex[8,31,36]. The parcellation patterns of the OrG (Fig. S4) and IPL (Fig. S26) in the MacBNA are consistent with existing cyto- or myeloarchitectonic atlases[18,47,48]. Compared with histological architecture, which characterizes local properties, anatomical connectivity can identify a finer parcellation since it takes advantage of long-range connections with the whole-brain, which could be consistent with the somatotopic and receptor organization. For example, the M1 is traditionally considered to be homogeneous within the area identified by architectonic studies[12,14], but our parcellation results for the M1 show a pattern along the ventral-dorsal axis that is consistent with that of the first and second gradients (Fig. S8) as well as with the somatotopic organization of the M1 area[49,50]. The premotor

cortex (PM) is another example in that it has 5 subregions in the traditional cytoarchitectonic atlas[18] but comprises 7 subregions in the MacBNA with 6DC segregated into dorsal and ventral parts and 6M divided into rostral and caudal parts. Some other studies reported similar subdivisions of 6DC and 6M using functional topology and receptor analysis[51,52]. Tracer studies[53,54] also showed a connectional divergence of the dorsal and ventral parts of 6DC in that the dorsal one had stronger connections with the superior parietal lobule and medial cingulate cortex, consistent with the structural connectivity obtained using tractography. Although gradient is another popular way to map brain regions in addition to parcellation[55–57], it provides an alternative aspect that can help to visualize and explain the parcellation pattern in the gradient space. Gradients characterized by connectivity were found to be in concordance with the neuronal granularity and myelination in the insula[58,59], implying that connectivity can capture microanatomical properties. Clear clusters in both structural and functional gradients space show the consistency between these two ways of mapping the brain (Fig. 3B, C). In summary, parcellations based on anatomical connectivity can provide fine-grained and biologically meaningful subdivisions of brain regions.

The MacBNA not only contains a fine parcellation of the whole macaque brain but also the detailed structural and functional connections of each subregion. Connections between brain regions identify the functional circuit that controls behavior and cognition[60,61] and are closely related to psychopathological diseases in humans. A recent invasive experiment using macaques revealed dissociable roles of the prefrontal-amygdala connections in social and nonsocial valuations[62]. Another human study using multiple sites found that the abnormal intrinsic and extrinsic circuits of the striatum provided a robust neuroimaging biomarker for the diagnosis of schizophrenia[63]. The identified heterogeneous connections between specific brain regions provide potential targets for treatments[64] and neuromodulations[65]. In addition, whole-brain connections allow for graph theory to be used to identify the functional subsystem of the brain and the network properties[66]. A recent modularity analysis using structural and functional connections showed that the salience network is anchored in the insula of mice as it is in macaques and humans[67,68]. Topological network analyses of the brain suggest the existence of modularity and hierarchy in a complex system. Using structural connections, the densely interlinked hub regions were identified as promoting global communication between modules in the cerebral cortex of macaques, thus showing similar properties of hub regions across primates[69,70]. It is interesting to consider how the distribution of the connections varies based on the network topology from a comparative view[71].

A Reference System for Spatial Coordinates

The fine-grained parcellation makes MacBNA a plausible reference for delineating a variety of profiles for each region. The MacBNA, which is based on MRI data, can become a valuable tool that will allow researchers to coordinate and integrate multi-modal data at different scales to elucidate details of brain anatomical structures. It is difficult to align data to 2D macaque atlases using modern image registration[44] so 3D MRI images and atlases are desirable as a bridge to link imaging, tracer, histological, and multi-omics information for any given brain space[10,43,72]. When dealing with huge multi-modal and multi-scale datasets, a biologically meaningful parcellation like MacBNA could be used as a prior to reduce the multi-modal and multi-scale data to low-dimension space, facilitating a study that integrates heterogeneous features[73–75]. Just as tracers can be used to identify subregions, as an anatomical connectivity-based parcellation, the MacBNA can also characterize differences in the regional connection between adjacent areas, making it a suitable reference system for targeting injection sites. Compared with using unguided or uniform samples, a well-designed injection strategy provides the maximal potential for revealing the connectional topography of the macaque brain while minimizing the number of animals sacrificed[76]. The connections based on the MacBNA showed a high consistency with those identified by tracers (r = 0.63) and seem to have a capacity that is comparable to that of tracer studies for capturing regional connectivity heterogeneity (Fig. 5C), implying that a connectivity-based atlas is suitable for guiding the injection of tracers. A fine-grained atlas also provides an accurate anatomical annotation of sample locations for multi-omics such as transcriptomes and proteomes. In multi-omics analyses, such as the identification of cell types and the enrichment of gene expression, unlike coarse macro-anatomical labeling, the MacBNA, comprising 304 subregions, could be used to coordinate the sampling spots precisely to ensure the coherence of samples across multiple specimens[77–79].

A Common and Cross-species Parcellation Pipeline for Comparison

The parcellation pipeline of the MacBNA has the potential to be applied across different species as it utilizes indirect and intact measurements of the brain that could be easily acquired in other species, allowing for rapid and efficient parcellations of brain regions using a common methodology. As post-mortem dMRI techniques advance, opportunities for collecting high spatial and angular resolution MR images covering the whole brain

from various animals, such as dogs, cats, monkeys, and great apes, will increase[80–84]. The protocols that we used for the preparation of tissues for the MRI acquisition could be generalized to other species ensuring the comparability of data. The parcellation pipeline is open to the public so that it could be utilized in any species or single brain region of interest using dMRI data. The accumulation of postmortem dMRI data from primates makes it possible to generalize the parcellation framework to construct connectivity-based atlases[80], facilitating a polygenetic comparison across primates. Canines or felines, being the most common animals accompanying humans, are highly social with each other and share a long evolutionary history with humans. A connectivity-based atlas with the parcellation pipeline in this study could provide the basis for investigating the mechanisms of co-evolution and social cognitions such as face recognition[85–87].

A review[88] pointed out the importance of comparing species in a common space, using the same regional resolution and similar features. We provide both a coarse level atlas with 58 initial region and a fine level one with 304 regions for different research purposes. The two versions share similar nomenclature with the Human Brainnetome Atlas[27], facilitating cross-species studies in a homologous target space. The coarse one could be adapted to evaluate mosaic evolution such as the disproportionate expansions of the cortex across primates[89]. The fine-grained one could be used to identify functional units that are potentially homologous with those of humans under comparative frameworks such as blueprints and activity correlation[90–92]. Since the Brainnetome Atlases in both humans and macaques have been completed, they offer a potential path for understanding brain evolution by comparative connectivities based on fine-grained brain parcellations across species. Many interesting topics related to evolutionary mechanisms, such as language and tool use, could be explored from the perspective of the Brainnetome Atlases[30,93,94].

Multi-modal and Multi-scale Dataset

The resource released in this study includes not only a new macaque atlas but also its corresponding structural and functional connectomes, as well as high-quality dMRI and Nissl-stained images with manual annotations of white and gray matter, making MacBNA a multi-scale multi-modal atlas resource. We collected extensive, high-quality (0.45 mm^3 and 180 diffusion directions with multiple shells) postmortem diffusion MRI data from 8 ex vivo macaques as well as ex vivo dMRI images and Nissl sections covering the whole brain (0.22 μm in plane, 139 slices) from a single subject in this study. High spatial resolution DWI images reduce PVE and

provide more precise reconstructions of white matter bundles[95–97]. Moreover, using multiple angular contrast, a multi-shell acquisition strategy, as we did can provide better estimates of different diffusion compartments and ensure a more accurate fit of the fiber orientation in a subsequent analysis[98].

The multi-modal and multi-scale data allow for the direct exploration of the relationship between various profiles for each region, i.e., the structural and functional connectivity, gradients, and cytoarchitecture (Figs. 3,4). Complementary cytoarchitecture and connectivity information about each brain region makes it possible to investigate the principles underlying the structural-functional convergences or discrepancies throughout the whole brain[1–5]. The included gradients pave a way to predict the hierarchy across the neocortex and identify the topographic organization of the subcortex[1,6,7]. Moreover, integrating the aforementioned characteristics of the brain based on a reference atlas allows for cross-validation by independent aspects of brain properties, such as the connections obtained using tracers, tractography, and the glial framework[8–10], leading to a deeper understanding of the biological mechanisms. Comparisons between non-invasive measurements such as in vivo brain imaging and invasive or ex vivo studies such as electrophysiology is exclusively possible in experimental animals, facilitating the medical translation to humans.

Meanwhile, a resource such as ours provides a database for exploring cutting-edge algorithms that can align information across multiple modalities and scales in a common reference space[14–16]. This resource will be an open-access platform for development of new fusion models such as BigBrain and PRIME-DRE[18,19]. Both supervised and unsupervised learning methods could be developed to investigate joint associations between multi-modal and multi-scale datasets, thus making the best use of the available information for underlying problems such as the association between imaging data and genetics in psychological diseases[99,100]. When facing the massive storage and super-computation of multi-modal and multi-scale brain data, developing efficient and fast fusion algorithms is an urgent need[17]. Cross-scale registration is another challenge when integrating information at different scales[45]. Manual annotations of the tissues, such as white matter and gray matter labeled by anatomical experts, provide the substrates for training and validation of supervised registration and segmentation models. Such an open-access resource can provide the substrates necessary to explore state-of-the-art models that can align MRI images to histological data.

Because a whole-brain connectome based on tracers is not available, the connectomes of the MacBNA could provide an alternative that can be used to power brain modelling and simulation. The empirical

connectomes identified by diffusion and functional MRI play a crucial role in virtual brain modelling where the spatial and temporal interactions of the simulation system depend on the neuroanatomical connections[101,102]. Large-scale brain models, such as mean-field models[103], which describe the collective action of populations of neurons, have found broad success in applications to many macroscopic activities, such as sleep, anesthesia, and resting state functional networks[104–106]. For region-based brain activity research, an accurate and reliable connectome will exert a substantial influence on the modelling results[107]. Since whole-brain dynamic models of rodents are readily available[108], a non-human primate model is necessary for cross-species comparison studies. As an initial step in constraining the brain models, the plausible connectome of the MacBNA could be incorporated into open-source simulation tools, such as The Virtual Brain[109,110] and Neurolib[111], facilitating the translation across rodents, nonhuman primates, and humans from the perspective of a digital twin brain.

Conclusion and Outlook

We present a new macaque brain atlas, the Macaque Brainnetome Atlas, based on connectivity with high spatial and angular resolution DWI images. The MacBNA consists of not only a plausible and fine-grained parcellation but also the detailed macroscopic connections of macaques. It can provide a reliable reference system for coordinating and integrating a variety of types of brain maps, i.e., not only the MRI and Nissl-stained data present in this study but also mesoscale connections, transcriptomes, and proteomes, which are major research themes in brain projects around the world. In addition, the proposed surface-based parcellation pipeline can be applied across species to construct a similar feature space for comparative research. Thus, we envision that the Macaque Brainnetome Atlas and the multi-modal multi-scale resource will play a role in neuroscience, translational medicine, and computational models.

Methods

Animals and Data Acquisition

Eight post-mortem monkeys (Brainnetome-8) were utilized to delineate the atlas and construct the structural

connectomes, and another open access cohort of 6 ex vivo subjects (Oxford-I) was used for validation. Two open access in vivo datasets (TVB and Oxford-II) were used to validate the structural connectomes and map the resting functional connectomes. Another female adult macaque was scanned to acquire the ex vivo dMRI and the Nissl-stained histological images covering the whole-brain. All animal procedures were approved by the Ethics Committee of the Biomedical Research of Institute of Automation, Chinese Academy of Sciences (No. IA-202032).

MRI of Brainnetome-8 and open access datasets

The Brainnetome-8 consisted of 2 male and 6 female (age = 5.6±1.06 years old) adult monkeys (*Macaca mulatta*). Each monkey was intraperitoneally injected with an overdose of pentobarbital. After a careful confirmation of deep anesthesia, a transcardial perfusion was performed with 500 ml of phosphate-buffered saline (PBS) solution containing 1% heparin (pH 7.4) and 0.1% gadolinium-diethylenetriamine pentaacetic acid (Gd-DTPA). After this 500 ml perfusion, the body organs such as the heart and bladder were removed, and the perfusion rate was decreased to 30 ml/min. This was followed by perfusing with a PBS solution containing 4% paraformaldehyde and 0.1% Gd-DTPA. After two hours of perfusion, the head was removed from the body, and the skull was carefully stripped to expose the whole brain. The formalin-fixed macaque brain was soaked in 0.1% Gd-DTPA and 0.1% sodium azide under sterile conditions for 4 weeks to reduce the T1 relaxation time. Prior to imaging, the specimens were transferred to an MRI compatible holder bundled with medical gauze and immersed in Fomblin (Solvay, Brussels, Belgium) to prevent dehydration and susceptibility artifacts; air bubbles on the brain surface were removed with an aspirator.

Ex vivo MRI data were acquired on an ultra-high field 9.4T horizontal animal scanner (Bruker Biospec 94/30 USR, Ettlingen, Baden-Württemberg). The gradients were equipped with slew rate of 4570 mT/m/ms and maximum strength 660 mT/m, and the radiofrequency (RF) transmission and reception were achieved with a 72 mm inner-diameter quadrature RF coil. The T2w image for each specimen was acquired with a 3D Turbo RARE sequence: TE = 36 ms, TR = 2000 ms, NEX = 6, matrix size = 240×180×267, resolution = 0.3×0.3×0.3 mm, FOV = 72.0×54.0×80.1 mm. The multi-shell dMRI was acquired with a 3D multi-segment echo planar imaging diffusion weighted sequence: TE = 23 ms, TR = 200 ms, bandwidth = 178.5 kHz, NEX = 7, matrix size = 148×120×160, resolution = 0.45×0.45×0.45 mm, FOV = 66.6×54.0×72.0 mm. For 7 of the 8 monkeys, a total

of 186 diffusion-weighted images (DWI) with 2 shells were collected, including 6 non-diffusion images for b = 0 s/mm^2, 60 directions for b = 2400 s/mm^2 and 120 directions for b = 4800 s/mm^2, with a total scan duration of about 243 hours. The scanning for the last monkey consisted of 6 b = 0 s/mm^2, 30 b = 2400 s/mm^2, and 90 b = 4800 s/mm^2 DWI data and lasted about 145 hours.

The Oxford-I (http://fcon_1000.projects.nitrc.org/indi/PRIME/oxford2.html) and Oxford-II (http://fcon_1000.projects.nitrc.org/indi/PRIME/oxford.html) datasets were both from an open resource PRIME-DE[3,112,113]. The Oxford-I dataset included 4 male and 2 female ex vivo subjects. Briefly, it consisted of 16 non-diffusion and 128 b = 4000 s/mm^2 volumes with 0.6 mm isotropic resolution. The Oxford-II dataset consisted of 20 male in vivo macaque monkeys with 0.5 mm isotropic T1w and 2 mm isotropic resting-state images. The in vivo TVB dataset was obtained from another public resource[110] that included 8 male macaque monkeys and consisted of 0.5 mm isotropic T1w images and 1.0 mm isotropic DWI data with 64 directions, b = 1000 s/mm^2.

MRI and Histology of R04

A postmortem macaque brain (ID: R04, female, 11 years old, 6.75 kg) was extracted and fixed following the protocol mentioned above. The brain was then scanned at 9.4T to acquire the whole-brain dMRI dataset with the same acquisition parameters as the Brainnetome-8 dataset except that the diffusion gradient directions were reduced to 30 for b = 2400 s/mm^2 and 90 for b=4800 s/mm^2. After the cerebellum was removed from the brain tissue, sucrose protection was utilized and the tissue was frozen with dry ice and embedded in optimal cutting temperature compound (OCT) before sectioning. Coronal sections with a thickness of 40 μm were obtained using a cryotome (Cryostar NX70, Thermo Fisher, United States) and block-face images were acquired for all sections using a camera. One in every 12 consecutive sections were selected for Nissl staining to visualize the cell bodies following the standard procedure. Each stained section was imaged with the microscopy (Axio Scan. Z1, Zeiss, Germany) at 0.22 μm in-plane resolution. For those sections with severe artifacts, whenever it was possible, the neighboring sections were chosen and stained as alternatives.

Preprocessing

For the ex vivo subjects, the T2w or b0 images were contrast inverted[34] as a fake T1w to reconstruct the surfaces via the HCP-NHP pipelines[114]; for the in vivo subjects, the surfaces were reconstructed using the T1w structural

images directly. Then those surface data were all resampled to 10k and 32k for the subsequent analysis. Additionally, the high-contrast b0 image of a post-mortem template named CIVM[115] was utilized to reconstruct the CIVM surface for the subsequent definition of seed regions (Fig. 1A).

Preprocessing of the diffusion MRI data was performed in the same way across all the subjects. Specifically, eddy current correction, unringing, and denoising were performed using FSL[116] and Mrtrix3[117]. Finally, fiber orientation distributions were estimated using Bedpostx in FSL. Specially, the averaged b0 images underwent intensity bias correction using N4BiasCorrect[118] for registration to the CIVM template.

A recently available fMRI pipeline[19] was adapted to preprocess the resting fMRI data. Briefly, it included despiking, motion correction, global scaling, and nuisance regression of the white matter (WM) and cerebrospinal fluid (CSF) signals, bandpass filtering (0.01–0.1 Hz), and co-registration to native anatomical space. Then the denoised resting fMRI data was projected to the CIVM midthickness surface and smoothed with FHWM = 3 mm.

The restacked 3D block-face image was used as the reference image space for the coregistration of the dMRI data. The Macaque Brainnetome Atlas was first non-linearly mapped to the R04 diffusion space and then linearly aligned to block-face space using the ANTs algorithm. A coarse linear alignment between the corresponding Nissl section and the block-face image roughly located the brain regions of the MacBNA, and the parcellations were then manually inspected and corrected.

Initial Seed Region Definition

The initial parcellation units of the macaque brain were mainly defined using the previous macaque atlases[16,18,115,119] or delineations of the macaque brain[120]. Splitting the cortical regions was based on landmarks, such as large sulci and gyri, accompanied by some cytoarchitecturally defined boundaries as a complement (Supplement Fig. S1, Tab. S1). The initial seed regions of the subcortex were solely determined by referring to Paxinos et al.'s[18] rhesus monkey brain atlas. All the regions were delineated in the CIVM template, and then the cortical ones were projected to the CIVM mid-surface to obtain a surface-based segmentation of 21 regions (Fig. 1A).

Surface-based Probabilistic Tractography and Connectivity-Based Parcellation

With 21 cortical seed regions delineated on the surface, a surface-based probabilistic tractography was performed using probtrackx2 in FSL. Taking an initial region as a seed mask (Fig. 1B), 10000 streamlines were sampled originating from each vertex, with a 0.2 curvature constraint, 3200 steps per sample, and a 0.5 mm step length. In addition, the pial surface of each subject was taken as a stop mask to prevent the streamline from crossing the sulci. Finally, a whole-brain connectivity matrix was constructed and smoothed to 2 mm to reduce the noise (Fig. 1C). A similarity matrix was derived from the connectivity matrix and then group-wise averaged. Spectral clustering was used to define the distinct subregions (Fig. 1D) as in our previous study of the human brain[27]. Subcortical regions were parcellated in a similar way, but using tracking in volume space. In addition to the hard parcellation, gradients of the seed region were derived from the similarity matrix using diffusion embedding[38] to explore the pattern of changes along specific directions as a complement to and explanation of the parcellation.

Strategies for Choosing Optimal Cluster Number and Hierarchical Parcellation

To obtain a reliable parcellation of each region, we selected the local peak as the optimal cluster number using a weighted score obtained by aggregating three characteristic cluster indices, Cramér's V (CV), topological distance (Tpd), and hierarchy index (Hi). These cluster indices were described in detail in Li et al.'s study[121]. An entropy-based aggregate method[122] was utilized to combine a pairwise CV between individuals, a group-level Tpd between hemispheres, and a group-level Hi of each hemisphere into one. The aggregate score of a cluster number *i* was computed according to:

$$score_i = \sum_j h_j \cdot M_{ij} \quad \begin{pmatrix} j = 1,2, \dots m \\ i = 2 \dots K \end{pmatrix} \tag{1}$$

where Mij is the value of cluster i of the jth index, and h_j is the weight of the jth index. Here, m is equal to 3 because CV, Tpd, and Hi were all three used, and K is the maximal cluster number. The weight h_j was computed as:

$$e_j = -\sum_{i=2}^{K} p_{ij} ln p_{ij} \tag{2}$$

$$h_j = \frac{1 - e_j}{\sum_{k=1}^{m}(1 - e_k)} \tag{3}$$

where p_{ij} *is* the normalized M_{ij} to ensure $\sum_{i=2}^{K} p_{ij} = 1$.

A hierarchical parcellation strategy was employed on three initial ROIs (i.e., IPL, STG, and CG). For example, the IPL was parcellated into a sulcal part with four subregions (IPLs) and a gyral part (IPLg) with only one subregion (Fig. 1F), to which the strategy of parcellation was applied again to obtain a finer pattern (Fig. S26).

Mapping to Volume and NMT Template

Because the parcellation of the cortex was defined on the brain surface, mapping to volume space was needed to provide for a more general application. Based on the characteristic of columnar anisotropy in the neocortex[28], each voxel was assigned to the label of its closest vertex along the direction perpendicular to the cortical surface. A manual correction and smoothing operation were applied to fix some errors, such as discontinuities or outliers of the parcellation. Since the new atlas was constructed on an ex vivo CIVM template, we also mapped it to the well-known NMT in vivo template[123] using a nonlinear registration provided by ANTs[124] so that our atlas could be used in either setting.

Structural/Resting Functional Connectivity and Gradients Analysis

For each voxel within a brain region of the MacBNA, a probabilistic tractography was performed to obtain its structural connectivity to the whole brain using 10000 samples. Then, we obtained the structural connectivity of a region with the whole brain by averaging the structural connectivity across all the voxels within it. A group-wise structural connectivity map was calculated by normalizing the connectivity of each subject to the standard space and then averaging across all the subjects.

The functional connectivity of each region with the whole brain was measured by the Pearson's correlation coefficient (Fisher's z-transformed) between its averaged preprocessed time series and that of each voxel of the whole brain. The averaged group-wise functional connectivity across subjects was tested for statistical significance with a one-sample *t* test (FDR corrected at $P < .01$).

Diffusion embedding[38] was performed on the similarity matrix between the connectivity of each voxel within the brain region. We selected the top 20 components with $\alpha = 3$ and $k = 10$ in the embedding algorithm and visualized the gradients with t-SNE[39] in a 2D dimension.

Structural and Resting Functional Connectome of MacBNA

The connectivity-based atlas provided the brain regions as nodes for constructing a whole-brain connectome. For the structural connectome, we nonlinearly warped the atlas to each subject's native space and then performed probabilistic tractography, as mentioned above, to count the connected streamlines as the weight of the edge between each pair. Finally, the connectome was log normalized and averaged across the subjects. For the resting functional connectome, the ROI-wise Pearson's correlation was calculated as the functional connection between regions and was then Fisher's *z*-transformed. A one-sample *t* test was used to determine the statistical significance on the group level (FDR corrected at $P < .01$). In addition, a seed-based correlation analysis was conducted on a posterior cingulate cortex region, CGdc, of the MacBNA to generate a correlation map of the default mode network in macaques.

Cytoarchitectonic analysis

The digitalized images of the Nissl-stained sections were used for the cytoarchitectonic analysis as Amunts et al.[10] did. Briefly, the images were down sampled to 22 μm and smoothed to reduce the noise and artifacts. The density profiles of the regions of interest were extracted orthogonally to the surface. The features extracted from the profiles were used to measure the distance between neighboring profiles[10,125]. A sliding window procedure (11 <= block size <= 24) determined the peak of the distance function. A Hotelling's T^2 test was used to confirm the statistical significance of the peak. The peak locations identified with multiple block sizes were also evaluated by comparison with maxima locations at neighboring stained sections to exclude the false positive peaks caused by artifacts or outliers (Figs. S3, S6).

Glial framework

The glial framework consisted of the orientation estimation and fiber tractography using Schurr and Mezer's[37] method. In short, a structure tensor analysis was used to fit the local fiber orientations according to the spatial distribution of the glial cells. The tile size was set at 44 microns (i.e., 200 pixels) with the $\rho = 15$ and $\sigma = 3$ as default. A white matter mask was generated using a semi-automatic annotation tool[126] based on the contrast between gray and white matter in each Nissl slice. The principal direction estimated using dtifit in FSL with

dMRI data of the same monkey was aligned to block-face space for comparison with the orientation obtained from the glial organization. The white matter pathway was reconstructed with the Fiber Assigned by Continuous Tracking[127], a deterministic tractography algorithm in Mrtirx3[117]. Step size was set at 3 voxels and the maximal angle was 60°. The seed mask was located in the white matter and 25 streamlines were seeded for each voxel.

Validation with Independent Dataset

Two independent datasets were used for validation in this study, (a) an ex vivo one with 6 subjects (Oxford-I) and (b) an in vivo one with 8 subjects (TVB). We validated the consistency of the parcellation pattern using Cramér's V coefficient[128] between the Brainnetome-8 and Oxford-I to ensure that the whole-brain parcellation was reproducible. We obtained three group-wise structural connectomes from the Brainnetome-8, Oxford-I, and TVB separately in the same way as above and validated their Pearson correlation to ensure the reliability and generality of the structural connectomes.

Validation with Tracer Data

Tracer-derived connectomes are the standard for validating a connectome constructed with diffusion MRI. An open tracer resource of macaque data[42,35] was adapted to evaluate the connectome defined by the Brainnetome-8 using tractography. First, we mapped the injection sites to the CIVM template surface to determine the target regions in our atlas. Nine target regions from Markov et al.[42] were excluded because the related injection sites did not satisfy a one-to-one mapping, i.e., multiple sites projected to the same region of our atlas or were located near the boundary. Then, the tracer connectome was mapped to our atlas simply based on the overlap ratio to the M132 parcellation of Markov et al.[42] This was possible because Donahue et al.[35] provided the tracer coordinates that Markov et al.[42] had used in their study, enabling us to compare our atlas with Markov et al.'s tracer data. Finally, a 20×20 subgraph was extracted from the transformed tracer-derived connection matrix to calculate the correlation with the dMRI ones. A two-sample *t* test was performed to compare the dMRI connections with the whole brain between a pair of regions as well as to compare the tracer-based connection via a direct subtraction of the connection strength.

Data and Code Availability

The ex vivo MRI data of the Brainnetom-8, the dMRI images and Nissl-stained sections of another postmortem monkey, and the code of the parcellation pipeline based on surface will be openly available at http://atlas.brainnetome.org upon acceptance.

Competing Interests Statement

The authors declare that they have no conflict of interest.

Acknowledgements

This work was partially supported by the Science and Technology Innovation 2030 - Brain Science and Brain-Inspired Intelligence Project (Grant No. 2021ZD0200200), Natural Science Foundation of China (Grant Nos. 82151307 and 31620103905), Strategic Priority Research Program of the Chinese Academy of Sciences (XDB32030207), and Science Frontier Program of the Chinese Academy of Sciences (grant No. QYZDJ-SSW-SMC019).

References

1. Van Essen, D. C. *et al.* Cerebral cortical folding, parcellation, and connectivity in humans, nonhuman primates, and mice. in *Proceedings of the National Academy of Sciences of the United States of America* vol. 116 26173–26180 (National Academy of Sciences, 2019).
2. Gray, D. T. & Barnes, C. A. Experiments in macaque monkeys provide critical insights into age-associated changes in cognitive and sensory function. *Proc. Natl. Acad. Sci.* **116**, 26247–26254 (2019).
3. Milham, M. P. *et al.* An Open Resource for Non-human Primate Imaging. *Neuron* **100**, 61-74.e2 (2018).
4. Autio, J. A. *et al.* Minimal specifications for non-human primate MRI: Challenges in standardizing and harmonizing data collection. *NeuroImage* **236**, 118082 (2021).
5. Hayashi, T. *et al.* The nonhuman primate neuroimaging and neuroanatomy project. *NeuroImage* **229**, 117726 (2021).
6. Van Essen, D. C. & Glasser, M. F. Parcellating Cerebral Cortex: How Invasive Animal Studies Inform Noninvasive Mapmaking in Humans. *Neuron* **99**, 640–663 (2018).
7. Eickhoff, S. B., Yeo, B. T. T. & Genon, S. Imaging-based parcellations of the human brain. *Nat. Rev. Neurosci.* **19**, 672–686 (2018).
8. Van Essen, D. C., Donahue, C., Dierker, D. L. & Glasser, M. F. Parcellations and Connectivity Patterns in Human and Macaque Cerebral Cortex. in *Micro-, Meso- and Macro-Connectomics of the Brain* (eds. Kennedy, H., Van Essen, D. C. & Christen, Y.) (Springer, 2016).
9. Caspers, S., Eickhoff, S. B., Zilles, K. & Amunts, K. Microstructural grey matter parcellation and its relevance for connectome analyses. *NeuroImage* **80**, 18–26 (2013).
10. Amunts, K. *et al.* BigBrain: An Ultrahigh-Resolution 3D Human Brain Model. *Science* (2013) doi:10.1126/science.1235381.
11. Alkemade, A. *et al.* A unified 3D map of microscopic architecture and MRI of the human brain. *Sci. Adv.* **8**, eabj7892.
12. Brodmann, K. Beitraege zur histologischen lokalisation der grosshirnrinde. IIIte mitteilung: Die rindenfelder der niederen affen. *J. Fuer Psychol. Neurol.* **4**, 177–226 (1905).

13. Walker, A. E. A cytoarchitectural study of the prefrontal area of the macaque monkey. *J. Comp. Neurol.* **73**, 59–86 (1940).

14. Lewis, J. W. & Van Essen, D. C. Mapping of architectonic subdivisions in the macaque monkey, with emphasis on parieto-occipital cortex. *J. Comp. Neurol.* **428**, 79–111 (2000).

15. Hartig, R. *et al.* The Subcortical Atlas of the Rhesus Macaque (SARM) for neuroimaging. *NeuroImage* **235**, 117996 (2021).

16. Saleem, K. S. & Logothetis, N. K. *A combined MRI and histology atlas of the rhesus monkey brain in stereotaxic coordinates*. (Amsterdam, The Netherlands, 2007).

17. Preuss, T. M. & Goldman-Rakic, P. S. Myelo- and cytoarchitecture of the granular frontal cortex and surrounding regions in the strepsirhine primate Galago and the anthropoid primate Macaca. *J. Comp. Neurol.* **310**, 429–474 (1991).

18. Paxinos, G., Huang, X.-F., Petrides, M. & Toga, A. The Rhesus monkey brain : in stereotaxic coordinates. *Fac. Health Behav. Sci. - Pap. Arch.* (2009).

19. Jung, B. *et al.* A comprehensive macaque fMRI pipeline and hierarchical atlas. *NeuroImage* **235**, 117997 (2021).

20. Johansen-Berg, H. *et al.* Changes in connectivity profiles define functionally distinct regions in human medial frontal cortex. *Proc. Natl. Acad. Sci.* **101**, 13335–13340 (2004).

21. Beckmann, M., Johansen-Berg, H. & Rushworth, M. F. S. Connectivity-based parcellation of human cingulate cortex and its relation to functional specialization. *J. Neurosci. Off. J. Soc. Neurosci.* **29**, 1175–1190 (2009).

22. Saygin, Z. M. *et al.* Anatomical connectivity patterns predict face selectivity in the fusiform gyrus. *Nat. Neurosci.* **15**, 321–327 (2012).

23. Osher, D. E. *et al.* Structural Connectivity Fingerprints Predict Cortical Selectivity for Multiple Visual Categories across Cortex. *Cereb. Cortex* **26**, 1668–1683 (2016).

24. Wu, D. *et al.* Hierarchy of Connectivity–Function Relationship of the Human Cortex Revealed through Predicting Activity across Functional Domains. *Cereb. Cortex* **30**, 4607–4616 (2020).

25. Passingham, R. E., Stephan, K. E. & Kötter, R. The anatomical basis of functional localization in the cortex. *Nat. Rev. Neurosci.* **3**, 606–616 (2002).

26. Liu, C. *et al.* Marmoset Brain Mapping V3: Population multi-modal standard volumetric and surface-based templates. *NeuroImage* **226**, 117620 (2021).

27. Fan, L. *et al.* The Human Brainnetome Atlas: A New Brain Atlas Based on Connectional Architecture. *Cereb. Cortex* **26**, 3508–3526 (2016).

28. Liu, C. *et al.* A digital 3D atlas of the marmoset brain based on multi-modal MRI. *NeuroImage* **169**, 106–116 (2018).

29. Cerliani, L., D'Arceuil, H. & Thiebaut de Schotten, M. Connectivity-based parcellation of the macaque frontal cortex, and its relation with the cytoarchitectonic distribution described in current atlases. *Brain Struct. Funct.* **222**, 1331–1349 (2017).

30. Cheng, L. *et al.* Connectional asymmetry of the inferior parietal lobule shapes hemispheric specialization in humans, chimpanzees, and rhesus macaques. *eLife* **10**, e67600 (2021).

31. Xia, X. *et al.* Fine-Grained Parcellation of the Macaque Nucleus Accumbens by High-Resolution Diffusion Tensor Tractography. *Front. Neurosci.* **13**, (2019).

32. He, B. *et al.* Fine-Grained Topography and Modularity of the Macaque Frontal Pole Cortex Revealed by Anatomical Connectivity Profiles. *Neurosci. Bull.* **36**, 1454–1473 (2020).

33. Schotten, M. T. de, Urbanski, M., Valabregue, R., Bayle, D. J. & Volle, E. Subdivision of the occipital lobes: An anatomical and functional MRI connectivity study. *Cortex* **56**, 121–137 (2014).

34. Ambrosen, K. S. *et al.* Validation of structural brain connectivity networks: The impact of scanning parameters. *NeuroImage* **204**, (2020).

35. Donahue, C. J. *et al.* Using diffusion tractography to predict cortical connection strength and distance: A quantitative comparison with tracers in the monkey. *J. Neurosci.* **36**, 6758–6770 (2016).

36. Li, K. *et al.* The human mediodorsal thalamus: Organization, connectivity, and function. *NeuroImage* **249**, 118876 (2022).

37. Schurr, R. & Mezer, A. A. The glial framework reveals white matter fiber architecture in human and primate brains. *Science* **374**, 762–767 (2021).

38. Xu, T. *et al.* Cross-species functional alignment reveals evolutionary hierarchy within the connectome. *NeuroImage* **223**, 117346 (2020).

39. van der Maaten, L.J.P. & Hinton, G.E. Visualizing High-Dimensional Data Using t-SNE. *J. Mach. Learn. Res.* **9**, 2579–2605 (2008).

40. Ghahremani, M., Hutchison, R. M., Menon, R. S. & Everling, S. Frontoparietal Functional Connectivity in the Common Marmoset. *Cereb. Cortex* **27**, 3890–3905 (2017).

41. Yeo, B. T. T. *et al.* The organization of the human cerebral cortex estimated by intrinsic functional connectivity. *J. Neurophysiol.* **106**, 1125–1165 (2011).

42. Markov, N. T. *et al.* A Weighted and Directed Interareal Connectivity Matrix for Macaque Cerebral Cortex. *Cereb. Cortex* **24**, 17–36 (2012).

43. Alkemade, A. *et al.* A unified 3D map of microscopic architecture and MRI of the human brain. *Sci. Adv.* **8**, eabj7892 (2022).

44. Schilling, K. G. *et al.* A Web-Based Atlas Combining MRI and Histology of the Squirrel Monkey Brain. *Neuroinformatics* **17**, 131–145 (2019).

45. Goubran, M. *et al.* Multimodal image registration and connectivity analysis for integration of connectomic data from microscopy to MRI. *Nat. Commun.* **10**, 5504 (2019).

46. Ding, S.-L. *et al.* Comprehensive cellular-resolution atlas of the adult human brain. *J. Comp. Neurol.* **524**, 3127–3481 (2016).

47. Niu, M. *et al.* Organization of the Macaque Monkey Inferior Parietal Lobule Based on Multimodal Receptor Architectonics. *NeuroImage* 117843 (2021) doi:10.1016/j.neuroimage.2021.117843.

48. Pandya, D. N. & Seltzer, B. Intrinsic connections and architectonics of posterior parietal cortex in the rhesus monkey. *J. Comp. Neurol.* **204**, 196–210 (1982).

49. Kaas, J. H. Evolution of columns, modules, and domains in the neocortex of primates. *Proc. Natl. Acad. Sci.* **109**, 10655–10660 (2012).

50. Young, N. A., Collins, C. E. & Kaas, J. H. Cell and neuron densities in the primary motor cortex of primates. *Front. Neural Circuits* **7**, (2013).

51. Rapan, L. *et al.* Multimodal 3D atlas of the macaque monkey motor and premotor cortex. *NeuroImage* **226**, 117574 (2021).

52. Matelli, M., Luppino, G. & Rizzolatti, G. Patterns of cytochrome oxidase activity in the frontal agranular cortex of the macaque monkey. *Behav. Brain Res.* **18**, 125–136 (1985).

53. Marconi, B. *et al.* Eye–Hand Coordination during Reaching. I. Anatomical Relationships between Parietal and Frontal Cortex. *Cereb. Cortex* **11**, 513–527 (2001).

54. Luppino, G., Rozzi, S., Calzavara, R. & Matelli, M. Prefrontal and agranular cingulate projections to the dorsal premotor areas F2 and F7 in the macaque monkey. *Eur. J. Neurosci.* **17**, 559–578 (2003).

55. Dong, H.-M., Margulies, D. S., Zuo, X.-N. & Holmes, A. J. Shifting gradients of macroscale cortical organization mark the transition from childhood to adolescence. *Proc. Natl. Acad. Sci.* **118**, (2021).

56. Vos de Wael, R. *et al.* BrainSpace: a toolbox for the analysis of macroscale gradients in neuroimaging and connectomics datasets. *Commun. Biol.* **3**, 103 (2020).

57. Blazquez Freches, G. *et al.* Principles of temporal association cortex organisation as revealed by connectivity gradients. *Brain Struct. Funct.* **225**, 1245–1260 (2020).

58. Cerliani, L. *et al.* Probabilistic tractography recovers a rostrocaudal trajectory of connectivity variability in the human insular cortex. *Hum. Brain Mapp.* **33**, 2005–2034 (2012).

59. Cao, L. *et al.* Structural connectivity gradient associated with a dichotomy reveals the topographic organization of the macaque insular cortex. 2022.03.18.484254 Preprint at https://doi.org/10.1101/2022.03.18.484254 (2022).

60. Caminiti, R. *et al.* Computational Architecture of the Parieto-Frontal Network Underlying Cognitive-Motor Control in Monkeys. *eNeuro* **4**, (2017).

61. Zhu, Z. *et al.* A substantia innominata-midbrain circuit controls a general aggressive response. *Neuron* **109**, 1540-1553.e9 (2021).

62. Pujara, M. S., Ciesinski, N. K., Reyelts, J. F., Rhodes, S. E. V. & Murray, E. A. Selective prefrontal-amygdala circuit interactions underlie social and nonsocial valuation in rhesus macaques. *J. Neurosci.* (2022) doi:10.1523/JNEUROSCI.0794-21.2022.

63. Li, A. *et al.* A neuroimaging biomarker for striatal dysfunction in schizophrenia. *Nat. Med.* **26**, 558–565 (2020).

64. Sydnor, V. J. *et al.* Cortical-subcortical structural connections support transcranial magnetic stimulation engagement of the amygdala. *Sci. Adv.* **8**, eabn5803 (2022).

65. Zhao, W. *et al.* Common abnormal connectivity in first-episode and chronic schizophrenia in pre- and post-central regions: Implications for neuromodulation targeting. *Prog. Neuropsychopharmacol. Biol. Psychiatry* **117**, 110556 (2022).

66. Park, H.-J. & Friston, K. Structural and Functional Brain Networks: From Connections to Cognition. *Science* **342**, 1238411 (2013).

67. Tsai, P.-J. *et al.* Converging Structural and Functional Evidence for a Rat Salience Network. *Biol. Psychiatry* **88**, 867–878 (2020).

68. Touroutoglou, A. *et al.* A ventral salience network in the macaque brain. *NeuroImage* **132**, 190–197 (2016).

69. van den Heuvel, M. P. & Sporns, O. Rich-club organization of the human connectome. *J. Neurosci. Off. J. Soc. Neurosci.* **31**, 15775–15786 (2011).

70. Harriger, L., van den Heuvel, M. P. & Sporns, O. Rich club organization of macaque cerebral cortex and its role in network communication. *PloS One* **7**, e46497 (2012).

71. Rilling, J. K. & van den Heuvel, M. P. Comparative Primate Connectomics. *Brain. Behav. Evol.* 170–179 (2018) doi:10.1159/000488886.

72. Hawrylycz, M. J. *et al.* An anatomically comprehensive atlas of the adult human brain transcriptome. *Nature* **489**, 391–399 (2012).

73. Zhao, B. *et al.* Common genetic variation influencing human white matter microstructure. *Science* **372**, eabf3736 (2021).

74. Grasby, K. L. *et al.* The genetic architecture of the human cerebral cortex. *Science* **367**, eaay6690 (2020).

75. Sjöstedt, E. *et al.* An atlas of the protein-coding genes in the human, pig, and mouse brain. *Science* **367**, eaay5947 (2020).

76. Lin, M. K. *et al.* A high-throughput neurohistological pipeline for brain-wide mesoscale connectivity mapping of the common marmoset. *eLife* https://elifesciences.org/articles/40042 (2019) doi:10.7554/eLife.40042.

77. Maynard, K. R. *et al.* Transcriptome-scale spatial gene expression in the human dorsolateral prefrontal cortex. *Nat. Neurosci.* **24**, 425–436 (2021).

78. Schmitz, M. T. *et al.* The development and evolution of inhibitory neurons in primate cerebrum. *Nature* **603**, 871–877 (2022).

79. Han, L. *et al.* Cell transcriptomic atlas of the non-human primate Macaca fascicularis. *Nature* **604**, 723–731 (2022).

80. Tendler, B. C. *et al.* The Digital Brain Bank, an open access platform for post-mortem imaging datasets. *eLife* **11**, e73153 (2022).

81. Yendiki, A. *et al.* Post mortem mapping of connectional anatomy for the validation of diffusion MRI. *NeuroImage* **256**, 119146 (2022).

82. Dyrby, T. B. *et al.* An ex vivo imaging pipeline for producing high-quality and high-resolution diffusion-weighted imaging datasets. *Hum. Brain Mapp.* **32**, 544–563 (2011).

83. Sébille, S. B., Rolland, A. S., Welter, M. L., Bardinet, E. & Santin, M. D. Post mortem high resolution diffusion MRI for large specimen imaging at 11.7 T with 3D segmented echo-planar imaging. *J. Neurosci. Methods* **311**, 222–234 (2019).

84. Bryant, K. L. *et al.* Organization of extrastriate and temporal cortex in chimpanzees compared to humans and macaques. *Cortex* **118**, 223–243 (2019).

85. Gross, M. Are dogs just like us? *Curr. Biol.* **25**, R733–R736 (2015).

86. Thompkins, A. M. *et al.* Dog–human social relationship: representation of human face familiarity and emotions in the dog brain. *Anim. Cogn.* **24**, 251–266 (2021).

87. Thompkins, A. M. *et al.* Separate brain areas for processing human and dog faces as revealed by awake fMRI in dogs (Canis familiaris). *Learn. Behav.* **46**, 561–573 (2018).

88. Mars, R. B., Jbabdi, S. & Rushworth, M. F. S. A Common Space Approach to Comparative Neuroscience. 18 (2021).

89. Garin, C. M., Garin, M., Silenzi, L., Jaffe, R. & Constantinidis, C. Multilevel atlas comparisons reveal divergent evolution of the primate brain. *Proc. Natl. Acad. Sci.* **119**, e2202491119 (2022).

90. Mars, R. B. *et al.* Whole brain comparative anatomy using connectivity blueprints. *eLife* **7**, (2018).

91. Mantini, D. *et al.* Interspecies activity correlations reveal functional correspondence between monkey and human brain areas. *Nat. Methods* **9**, 277–282 (2012).

92. Hori, Y. *et al.* Interspecies activation correlations reveal functional correspondences between marmoset and human brain areas. *Proc. Natl. Acad. Sci.* **118**, (2021).

93. Xia, X., Gao, F. & Yuan, Z. Species and individual differences and connectional asymmetry of Broca's area in humans and macaques. *NeuroImage* **244**, 118583 (2021).

94. Wen, H., Xu, T., Wang, X., Yu, X. & Bi, Y. Brain intrinsic connection patterns underlying tool processing in human adults are present in neonates and not in macaques. *NeuroImage* **258**, 119339 (2022).

95. Sotiropoulos, S. N. *et al.* Advances in diffusion MRI acquisition and processing in the Human Connectome Project. *NeuroImage* **80**, 125–143 (2013).

96. Heidemann, R. M., Anwander, A., Feiweier, T., Knösche, T. R. & Turner, R. k-space and q-space: Combining ultra-high spatial and angular resolution in diffusion imaging using ZOOPPA at 7T. *NeuroImage* **60**, 967–978 (2012).

97. Liu, C. *et al.* A resource for the detailed 3D mapping of white matter pathways in the marmoset brain. *Nat. Neurosci.* **23**, 271–280 (2020).

98. Jbabdi, S., Sotiropoulos, S. N., Savio, A. M., Graña, M. & Behrens, T. E. J. Model-based analysis of multishell diffusion MR data for tractography: How to get over fitting problems. *Magn. Reson. Med.* **68**, 1846–1855 (2012).

99. Du, L. *et al.* Detecting genetic associations with brain imaging phenotypes in Alzheimer's disease via a novel structured SCCA approach. *Med. Image Anal.* **61**, 101656 (2020).

100. Peng, P. *et al.* Group Sparse Joint Non-Negative Matrix Factorization on Orthogonal Subspace for Multi-Modal Imaging Genetics Data Analysis. *IEEE/ACM Trans. Comput. Biol. Bioinform.* **19**, 479–490 (2022).

101. Breakspear, M. Dynamic models of large-scale brain activity. *Nat. Neurosci.* **20**, 340–352 (2017).

102. Deco, G., Jirsa, V. K. & McIntosh, A. R. Emerging concepts for the dynamical organization of resting-state activity in the brain. *Nat. Rev. Neurosci.* **12**, 43–56 (2011).

103. Jirsa, V. K. & Haken, H. Field Theory of Electromagnetic Brain Activity. *Phys. Rev. Lett.* **77**, 960–963 (1996).

104. Phillips, A. J. K. & Robinson, P. A. A quantitative model of sleep-wake dynamics based on the physiology of the brainstem ascending arousal system. *J. Biol. Rhythms* **22**, 167–179 (2007).

105. Bojak, I. & Liley, D. T. J. Modeling the effects of anesthesia on the electroencephalogram. *Phys. Rev. E Stat. Nonlin. Soft Matter Phys.* **71**, 041902 (2005).

106. Deco, G., Jirsa, V., McIntosh, A. R., Sporns, O. & Kötter, R. Key role of coupling, delay, and noise in resting brain fluctuations. *Proc. Natl. Acad. Sci.* **106**, 10302–10307 (2009).

107. Domhof, J. W. M., Jung, K., Eickhoff, S. B. & Popovych, O. V. Parcellation-induced variation of empirical and simulated brain connectomes at group and subject levels. *Netw. Neurosci.* **5**, 798–830 (2021).

108. Melozzi, F., Woodman, M. M., Jirsa, V. K. & Bernard, C. The Virtual Mouse Brain: A Computational Neuroinformatics Platform to Study Whole Mouse Brain Dynamics. *eNeuro* **4**, ENEURO.0111-17.2017 (2017).

109. Sanz Leon, P. *et al.* The Virtual Brain: a simulator of primate brain network dynamics. *Front. Neuroinformatics* **7**, (2013).

110. Shen, K. *et al.* A macaque connectome for large-scale network simulations in TheVirtualBrain. *Sci. Data* **6**, 123 (2019).

111. Cakan, C., Jajcay, N. & Obermayer, K. neurolib: A Simulation Framework for Whole-Brain Neural Mass Modeling. *Cogn. Comput.* (2021) doi:10.1007/s12559-021-09931-9.

112. Folloni, D. *et al.* Dichotomous organization of amygdala/temporal-prefrontal bundles in both humans and monkeys. *eLife* **8**, (2019).

113. Noonan, M. P. *et al.* A Neural Circuit Covarying with Social Hierarchy in Macaques. *PLOS Biol.* **12**, e1001940 (2014).

114. Autio, J. A. *et al.* Towards HCP-Style Macaque Connectomes: 24-Channel 3T Multi-Array Coil, MRI Sequences and Preprocessing. *NeuroImage* 116800 (2020) doi:10.1016/j.neuroimage.2020.116800.

115. Calabrese, E. *et al.* A diffusion tensor MRI atlas of the postmortem rhesus macaque brain. *NeuroImage* **117**, 408–416 (2015).

116. Woolrich, M. W. *et al.* Bayesian analysis of neuroimaging data in FSL. *NeuroImage* **45**, S173–S186 (2009).

117. Tournier, J.-D. *et al.* MRtrix3: A fast, flexible and open software framework for medical image processing and visualisation. *NeuroImage* **202**, 116137 (2019).

118. Tustison, N. J. *et al.* N4ITK: Improved N3 bias correction. *IEEE Trans. Med. Imaging* **29**, 1310–1320 (2010).

119. Reveley, C. *et al.* Three-Dimensional Digital Template Atlas of the Macaque Brain. *Cereb. Cortex* **27**, 4463–4477 (2016).

120. Rushmore, R. J. *et al.* MRI-based Parcellation and Morphometry of the Individual Rhesus Monkey Brain: the macaque Harvard-Oxford Atlas (mHOA), a translational system referencing a standardized ontology. *Brain Imaging Behav.* (2020) doi:10.1007/s11682-020-00357-9.

121. Li, H. *et al.* ATPP: A Pipeline for Automatic Tractography-Based Brain Parcellation. *Front. Neuroinformatics* **11**, (2017).

122. Zhu, Y., Tian, D. & Yan, F. Effectiveness of Entropy Weight Method in Decision-Making. *Math. Probl. Eng.* **2020**, e3564835 (2020).

123. Seidlitz, J. *et al.* A population MRI brain template and analysis tools for the macaque. *NeuroImage* **170**, 121–131 (2018).

124. Avants, B. B., Tustison, N. J., Wu, J., Cook, P. A. & Gee, J. C. An Open Source Multivariate Framework for n-Tissue Segmentation with Evaluation on Public Data. *Neuroinformatics* **9**, 381–400 (2011).

125. Zilles, K., Schleicher, A., Palomero-Gallagher, N. & Amunts, K. 21 - Quantitative Analysis of Cyto- and Receptor Architecture of the Human Brain. in *Brain Mapping: The Methods (Second Edition)* (eds. Toga, A. W. & Mazziotta, J. C.) 573–602 (Academic Press, 2002). doi:10.1016/B978-012693019-1/50023-X.

126. Hao, Y. *et al.* EdgeFlow: Achieving Practical Interactive Segmentation with Edge-Guided Flow. *ArXiv210909406 Cs* (2021).

127. Mori, S., Crain, B. J., Chacko, V. P. & van Zijl, P. C. Three-dimensional tracking of axonal projections in the brain by magnetic resonance imaging. *Ann. Neurol.* **45**, 265–269 (1999).

128. Cramér, H. *Mathematical Methods of Statistics (PMS-9), Volume 9. Mathematical Methods of Statistics (PMS-9), Volume 9* (Princeton University Press, 2016).

Figures

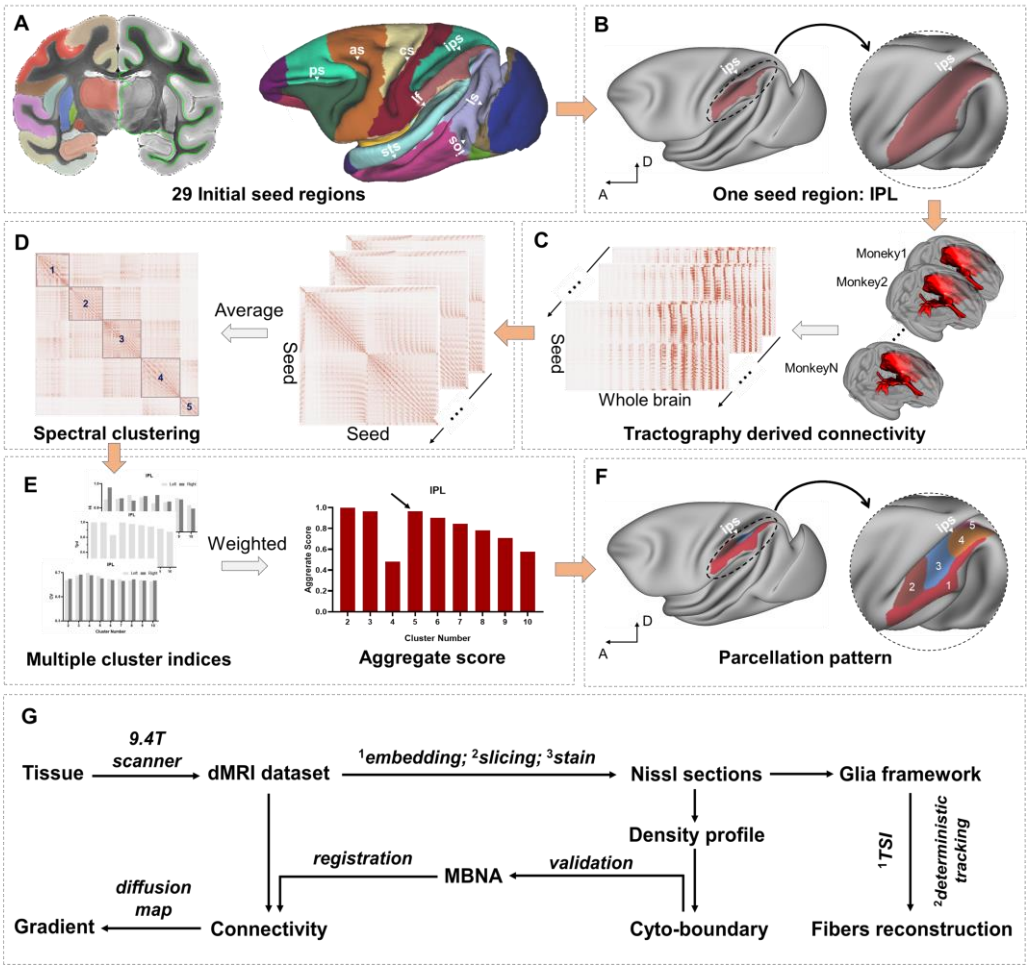

Fig. 1 The parcellation pipeline for the construction of the Macaque Brainnetome Atlas based on anatomical connectivity. (A) 29 initial seed regions of interest (ROIs), including 21 cortical and 8 subcortical regions, were manually delineated in volume space. The coronal view of the template brain shows the location of the anatomical seed regions as colored areas (left half of the slice) and as green lines on the white-to-gray surface (right half of the slice). Those seed regions were then mapped to the surface space to get surface-based ROIs for the cortical parcellation. (**B-F)** Surface-based parcellation of an exemplar seed region, the IPL. **(C)** Probabilistic tractography was performed from the seed to the whole brain and the connectivity information was stored in a connectivity matrix (seed-by-whole brain) for each subject. **(D)** Pairwise correlations of voxels in the seed region were calculated to get a similarity matrix (seed-by-seed) for each subject, and spectral clustering was conducted on the averaged similarity matrix across all subjects. **(E)** Three indices, CV, Tpd, and Hi, were fused to form an aggregate score based on entropy theory to estimate the optimal cluster number (5 was the optimal cluster number as indicated by the location of the peak) **(F)** The parcellation pattern of the IPL. **(G)** The protocol for acquiring the Nissl-stained data, and the exemplar joint study of our MRI and the Nissl images including the connectivity, gradients, cytoarchitecture analysis, and glia framework. Abbreviation: *as, arcuate sulcus; cs, central sulcus; ps, principal sulcus; lf, lateral fissure; sts, superior temporal sulcus; ls, lunate sulcus;*

cgs, cingulate sulcus; ots, occipitotemporal sulcus; pos, parieto-occipital sulcus; iocs, inferior occipital sulcus; *IPL, inferior parietal lobule.*

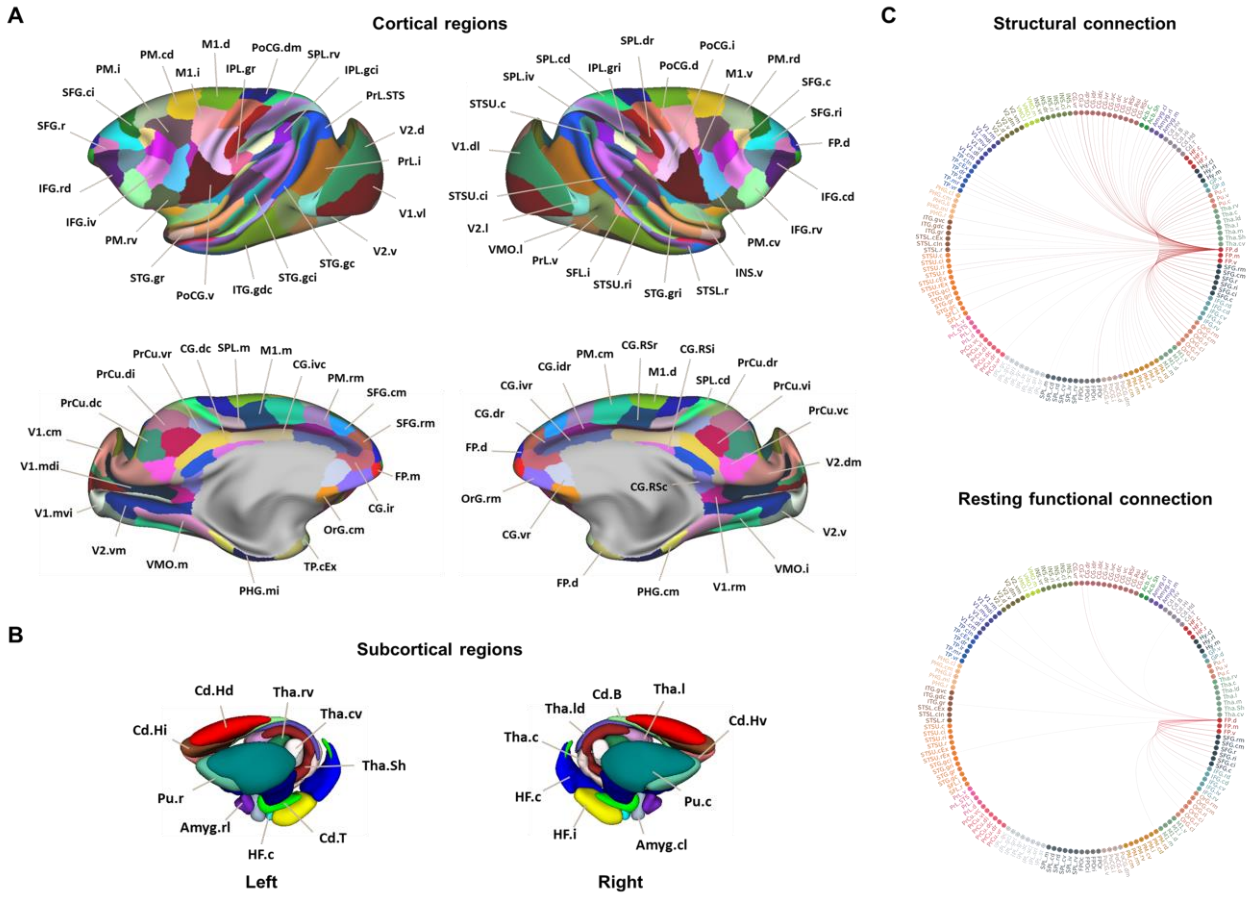

Fig. 2 Overview of the Macaque Brainnetome Atlas. (A) Surface view of 248 cortical regions and **(B)** 3D view of 56 subcortical regions. **(C)** The left intra-hemisphere structural and resting functional connection of an exemplar region, FPd. The nomenclature information for each subregion is listed in the Supplemental Nomenclature. The atlas is available at http://atlas.brainnetome.org. Abbreviation: *FPd, frontal pole dorsal part*.

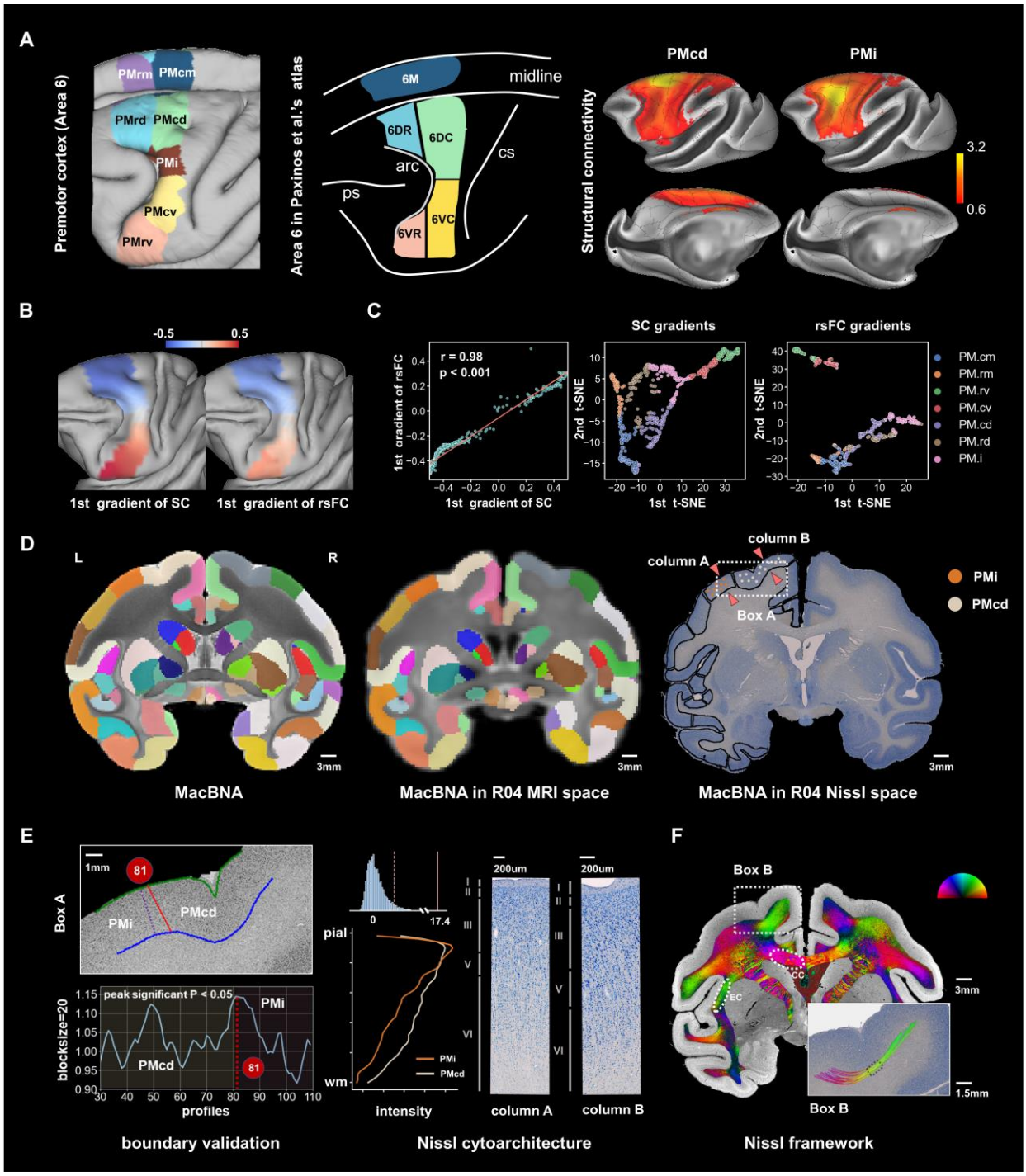

Fig. 3 Macaque Brainnetome Atlas of the premotor cortex (PM) and the exemplar joint study with the MRI and Nissl images. (A) Left panel shows the parcellation of the PM in the MacBNA, which subdivided it into 7 regions. Middle panel is the parcellation of the PM in Paxinos et al.'s atlas, which subdivided it into 5 subregions. Right panel is the structural connectivity of the PMcd and PMi with the whole brain. **(B)** The first gradient of the structural and resting-state functional connectivity of the PM. **(C)** The correlation between the two gradients and the visualization of the 7 clusters of the PM with the t-SNE. **(D)** Parcellations of the MacBNA in template, R04 MRI, and R04 Nissl space. The orange and gray dots mark the regions of the PMi and PMcd respectively. **(E)** The zoom-in details **(marked with white box)** indicate the boundary between the PMcd and PMi of the MBAN (purple line) based on connectivity and the boundary (red line) determined using a

quantitative cytoarchitecture analysis (left bottom). The middle panel is the mean density profile of the PMcd and PMi regions, and a permutation test with 5000 samples indicates the significant difference between their profiles ($P < .001$). The right panel shows the detailed laminar structures of two selected columns of the two regions that were marked in (D). **(F)** The fiber orientation reconstructed with the glial framework at a mesoscale spatial resolution (44 microns), and the white circles indicate two major tracts, i.e., CC and EC. The right bottom shows a tiny U-fiber connecting the neighboring gyral regions when seeding from the region below the sulci (black dotted box). Abbreviations: *PM, premotor cortex; PMrd, premotor cortex rostrodorsal part; PMcd, premotor cortex caudodorsal part; PMi, premotor cortex intermediate part; PMcv, premotor cortex caudoventral part; PMrv, premotor cortex rostroventral part; PMmr, premotor cortex rostromedial part; PMcm, premotor cortex caudomedial part. CC,* c*orpus callosum; EC, external capsules.* The abbreviations of the cytoarchitecture atlas come from Paxinos et al.'s study[18].

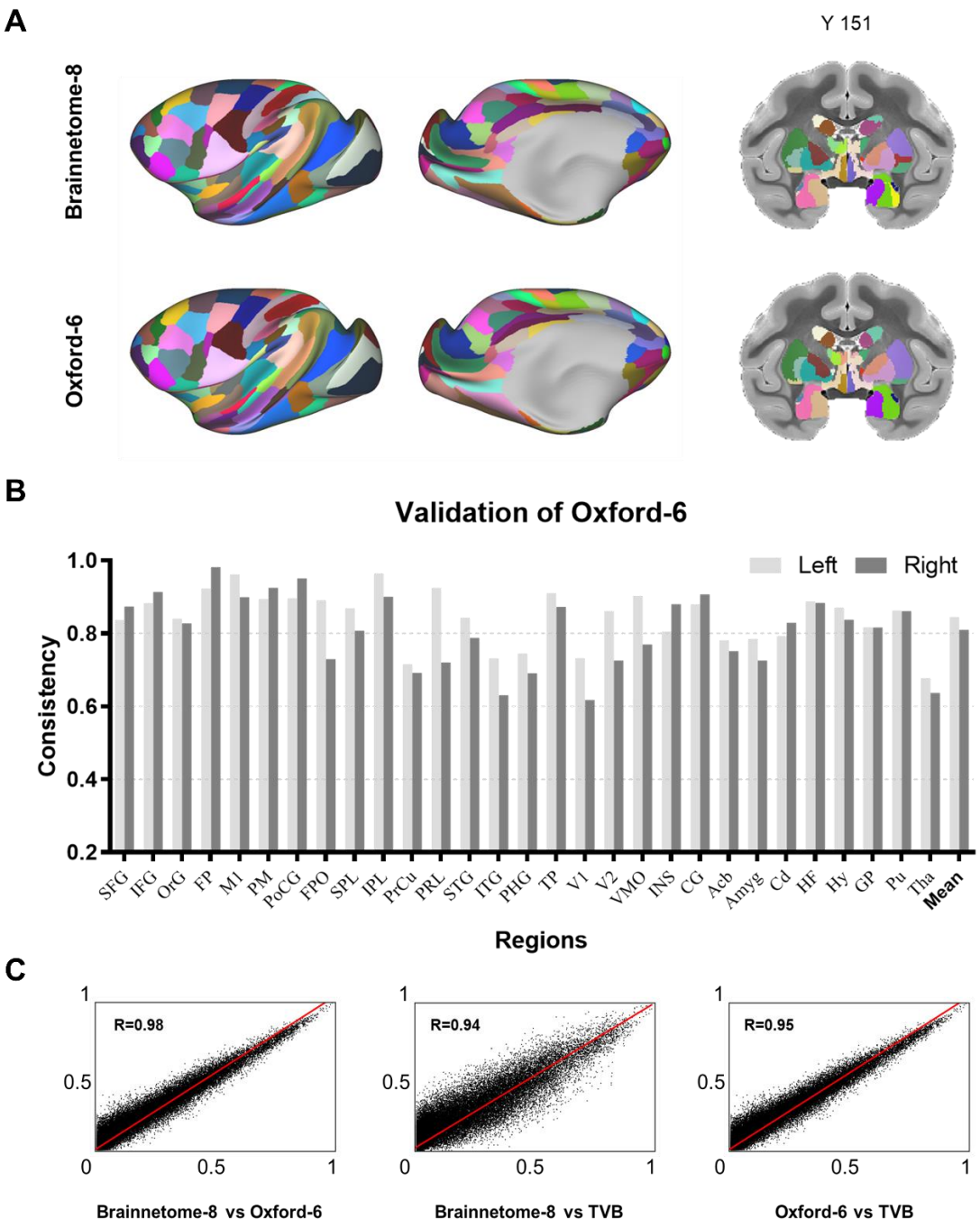

Fig. 4 Validation using independent datasets. (A) Overview of the parcellation of the whole brain using the Brainnetome-8 and Oxford-6 ex vivo datasets. **(B)** The consistency of each initial ROI between the two datasets. Most of the ROIs exceeded 0.7, indicating a high reproducibility. The mean was above 0.8 for both hemispheres. **(C)** The robustness of the structural connectomes with the new atlas as nodes in the three datasets, including an in vivo dataset. The Pearson correlation coefficients between each pair of datasets were all greater than 0.9 with *P* values smaller than 10^{-6}.

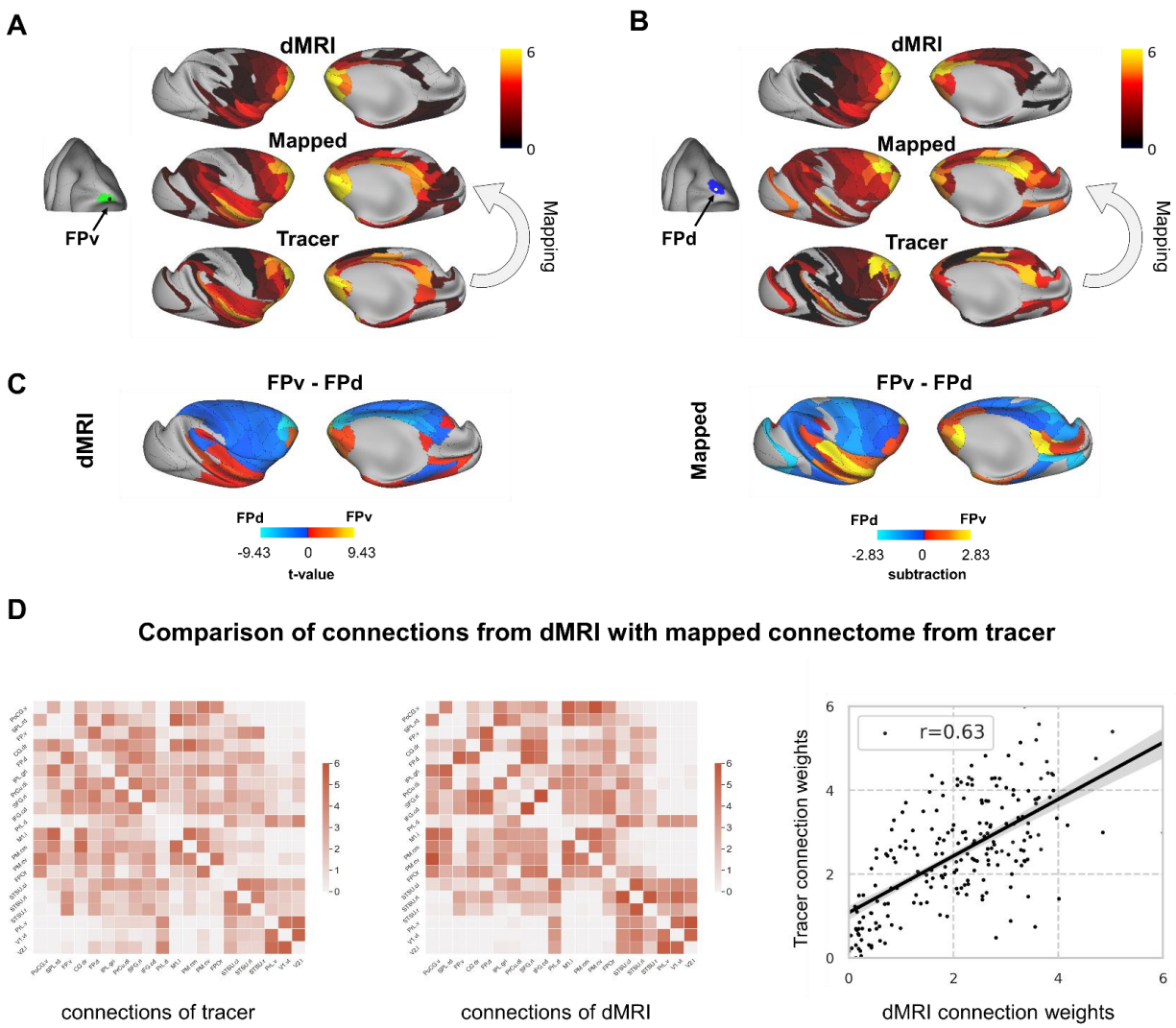

Fig. 5 Validation of the connectomes using tracer data. (A) In the left panel**,** the solid dots indicate the location of the injection sites in the MacBNA (FPv). In the right panel, the bottom row shows the original connection of the tracers from Markov et al.'s[42] tracer study. The middle row shows the tracer connections mapped to the MacBNA because we defined the original ones based on their atlas, which has 91 regions. The top row shows the dMRI-derived connections constructed from the tractography of FPv. **(B)** The same as **(A)** except that the injection site was located in FPd of the MacBNA. **(C)** The *t* value of two-sample *t* test between the brain-wide connections of FPv and FPd as revealed by dMRI in the left panel. Subtraction of the mapped brain-wide tracer connection of FPv from FPd in the right panel. **(D)** The connection matrix of 20 injected areas with each other. The left panel shows the mapped tracer connections from the original tracer study, the middle shows the dMRI-derived connections, and the right shows that the moderate correlation between the two matrixes was 0.63 with a *P* value smaller than 10^{-4}. Abbreviations: *FPv, frontal pole ventral part; FPd, frontal pole dorsal part.*